System integration and radiation pattern measurements of a phased array antenna employing an integrated photonic beamformer for radio astronomy applications

Maurizio Burla,[1,*] Chris G. H. Roeloffzen,[1] Leimeng Zhuang,[1] David Marpaung,[1] Muhammad Rezaul Khan,[1] Peter Maat,[2] Klaas Dijkstra,[2] Arne Leinse,[3] Marcel Hoekman,[3] and René Heideman[3]

[1]Telecommunication Engineering Group, CTIT Research Institute, University of Twente, P.O. Box 217, 7500 AE, Enschede, The Netherlands

[2]ASTRON, Oude Hoogeveensedijk 4, 7991 PD, Dwingeloo, The Netherlands

[3]LioniX B.V., PO Box 456, 7500 AL Enschede, The Netherlands

*Corresponding author: m.burla@ewi.utwente.nl

Received 24 August 2011; revised 28 November 2011; accepted 28 November 2011; posted 7 December 2011 (Doc. ID 152034); published 17 February 2012

In this paper we describe the system integration and the experimental demonstration of a photonically beamformed four-element receiving array antenna for radio astronomy applications. To our knowledge, the work described here is the first demonstration of the squint-free, continuously tunable beamsteering capability offered by an integrated photonic beamformer based on optical ring resonator true-time-delay units, with measured radiation patterns. The integrated beamformer is realized in a low loss, complementary metal-oxide-semiconductor (CMOS) compatible optical waveguide technology. The measurements show a wideband, continuous beamsteering operation over a steering angle of 23.5 degrees and an instantaneous bandwidth of 500 MHz limited only by the measurement setup.

OCIS codes: 070.1170, 070.5753, 130.0130, 130.6622, 060.5625, 280.5110.

1. Introduction

Large instantaneous bandwidth is a characteristic of great interest in many fields of application of wireless technology. In radio astronomy, in particular, the bandwidth of the receiver is an important aspect from several perspectives. First of all, sensitivity, defined as the minimum detectable apparent temperature variation of the scenario observed by the antenna, is inversely proportional to the square root of the bandwidth and the integration time [1]. Thus, it is desirable to have receivers with a band that is as wide as possible. In addition to that, in the radio astronomy science cases where survey speed is important, wide band is desired, because it leads to a wide velocity coverage and, in turn, to a larger volume of space surveyed per observation [2].

Phased array antennas are very flexible tools that are recently growing in popularity in the field of radio astronomy [3]. The need for wide instantaneous bands, together with the spread of phased array antenna technology in many fields of radio

1559-128X/12/070789-14$15.00/0

science, has drawn attention also to the development of wideband solutions for the beamformer section of the antenna system, which is the component that determines the desired phase and amplitude excitations to the individual antenna elements.

Several authors have shown how optical beamforming can be an advantageous solution in many cases where high performance applications are needed, due to the inherent advantages of photonic technology [4–8]. For example, optical fibers can be used to overcome the limitations in terms of weight, flexibility, size, cost, bandwidth, attenuation, and frequency dispersion of electronic feed networks. Notably, the last two advantages make them suitable for delay generation for beamsteering and phase reference distribution to large arrays [6,9]. Optical technology also allows higher electro-magnetic interference (EMI) immunity [9,10], and the possibility to optically multiplex different functions in the same network provides further benefit in the aspects described above [6,11,12].

In array beamformers, delay lines are the main constituting elements. When realized optically, they can offer wideband, continuously tunable operation, and can be made independent of the operating RF frequency [13–16], allowing squint-free beamsteering and controllable nulls positioned on large percentage bandwidths [4,16–20]. Multibeam capability can also be easily added to a beamformer, without dramatically increasing the network complexity, by using multiple optical wavelengths (as shown in [18,21–24]).

Nonetheless, in most cases, some of those advantages are often achieved at the expense of others. For example, some applications show wideband operation but offer only discrete delay values [25–28], or other examples show that the beamformer can become relatively bulky when based on fibers or free-space optical components [7,8,18,23].

In general, it is difficult to simultaneously achieve seamless tunability with a high delay–bandwidth product. Optical ring resonators (ORRs) are structural slow light devices that can provide continuously tunable delays, are independent of the RF operating frequency, and that offer no inherent limitations either in the percentage bandwidth (the bandwidth does not depend on the absolute RF frequency) or in the amount of achievable delay, since the delay–bandwidth product can be increased simply by cascading multiple basic delay elements.

ORRs can be implemented in photonic integrated circuits. This approach becomes very attractive in those applications where cost, weight, and compactness are important [29–31]. In our previous work [13,14,32], we proposed a solution that brings together many of the possible advantages of photonic beamforming: a fully programmable integrated optical beamformer, based on ORR delay units and filters. The performance of these types of components as delay elements has been demonstrated by several authors [32–34]. This solution, based on a low cost, complementary metal-oxide-semiconductor (CMOS) compatible process, is compact and lightweight. This makes it suitable for integration in airborne or spaceborne applications, where the current trend toward lower fuel consumption and the development of micro- and nanosatellites makes the aspects above more and more important. Integrating the combining and delaying functions in a single optical chip, this approach can be much cheaper and lighter than those based on discrete free-space or fiber-based components [30,31].

We first presented our approach in [13,14,32] by experimentally demonstrating the capabilities of the optical beam forming network (OBFN) subsystem. In this paper we show the system integration of the microwave photonic beamformer in a complete integrated antenna system demonstrator. In this paper we show the capabilities of the integrated system, providing measured radiation patterns. The employed antenna array is a modified version of a demonstrator previously equipped with a full electronic beamformer (EMBRACE, Electronic Multi Beam Radio Astronomy Concept) [35,36].

This paper is an extension of the work reported in [17]. New measurement results are presented. A comprehensive description of the system setup and of the tuning and measurement procedure is provided, together with a more complete discussion of the measured results. Furthermore, additional simulated antenna patterns are added to the measurements to show the effect of true time delay compared to the case of phase shifting.

The paper is organized as follows. In Section 2, after a brief theoretical introduction motivating the need for wideband delay units, we describe the optical components used for the delay and combining functions, and how they are assembled to create a complete beamformer network. Section 3 describes the integration of the beamformer in a complete RF photonic system. Section 4 explains the OBFN tuning procedure used to obtain the measured radiation pattern, which is shown and discussed in Section 5.

2. Beamformer based on Integrated Optical Ring Resonators

A. Beamforming Theory and Requirements for Wideband Operation

Phased array antenna technology allows fast and accurate beam pattern shaping and reconfigurability through the use of a so-called beamforming network. A beamformer can be generally defined as a network capable of generating the desired amplitude and phase excitations at each specific antenna element of the array. The relation between the radiation pattern and the excitation of the individual antenna elements is described below.

The array factor of an N element array, where we assume identical antennas with the same orientation, is related to the excitation of the individual elements of the array by the following expression [37]:

$$F(\vartheta,\phi)=\sum_{i=1}^{N} C_i \exp(j\alpha_i + jk_0\boldsymbol{\alpha_r}\cdot\mathbf{r_i}). \quad (1)$$

C_i and α_i represent the amplitude and the phase excitation of the ith element of the N elements array, respectively. $\boldsymbol{\alpha_r}$ is the vector defining the position of the observer, and $\mathbf{r_i}$ is the position of the ith antenna element with respect to the origin of the reference coordinate system. The array factor thus describes the effect of the spatial arrangement (given by the geometrical layout of the array, $\boldsymbol{\alpha_r}\cdot\mathbf{r_i}$) and of the complex amplitude excitation (C_i,α_i) of each individual antenna element forming the array. Since the complex excitations are defined by the input–output responses of the beamforming network, the ability to reconfigure those responses allows us, in turn, to accordingly modify the radiation pattern as desired.

For wideband operation, the phase term α_i should satisfy the specific condition of being a linear function of frequency in the band of interest:

$$\alpha_i = -k_0 L_i = -\frac{2\pi f}{c_0} L_i, \quad (2)$$

where c_0 is the speed of light in the medium, and L_i is the distance of the ith element from the plane passing by the origin and orthogonal to the desired pointing direction. Note that condition (2) coincides with the case in which the desired phase shift (at frequency f) is introduced by an ideal delay line of length L_i and propagation constant k_0. When this condition holds, the beam pointing is constant with frequency and wideband, meaning squint-free operation is achieved.

B. Delay Elements

The desired wideband characteristic for a delay unit expressed in Eq. (2) can be obtained by using a physical delay line. This is usually a bulky solution and, most importantly, it does not easily allow continuous tunability. The latter characteristic is needed to be able to generate an arbitrary beam pointing direction, which is of primary importance in many applications, namely, radio astronomy, mobile personal communications, or satellite reception. Several examples using chirped fiber gratings (CFGs) have been proposed that take advantage of photonic technology to achieve this desirable property [38–40].

As described in Section 1, an extremely compact and very effective way of implementing continuous tunability for a delay line is to exploit the properties of optical filters based on ring resonators [32–34]. In Fig. 1, the basic principle of approximating the linear phase response versus frequency of an ideal delay line (dashed line) by using the phase response of an ORR is illustrated. The slope of the phase response of an ORR (solid line in Fig. 1) can be tuned by varying the coupling coefficient to the input–output waveguide, and the center frequency by the optical phase shift in the ring waveguide. This can be done in such

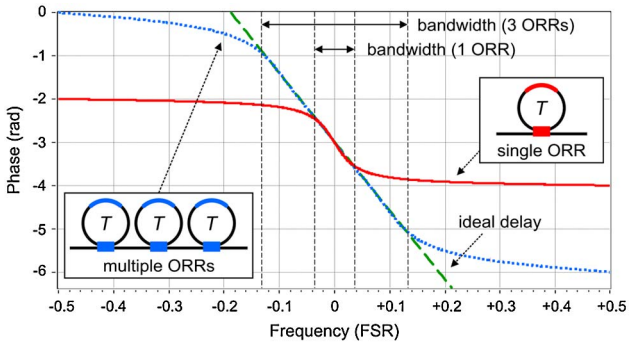

Fig. 1. (Color online) Phase response comparison: single ORR (solid), 3 ORRs (dotted), ideal delay line (dashed). In the insets: schematics of the single and multiple ORR delay elements.

a way to approximate the phase response of an ideal delay line over a specified bandwidth, as shown in Fig. 1, with a phase error ε below a maximum acceptable amount. A proper choice of the maximum value for ε ensures a negligible effect of the phase error on the pointing direction of the produced beam pattern, as analyzed in [41,42] for the specific case of CFG-based photonic beamformers.

ORRs can be conveniently modeled as digital filters [43] and exhibit a periodic frequency response. The free spectral range (FSR) is determined by the circumference of the ORR, and is equal to the reciprocal of the round trip time T. The frequency scale of Fig. 1 is normalized to the FSR. The use of ORRs offers another advantage when such components are employed as delay elements. Because of their full tunability, it is possible to cascade more units and tune them in order to approximate the desired phase response over a wider bandwidth (dotted line in Fig. 1), with no inherent percentage bandwidth limitation. Examples of this concept are also explained in [13,14].

C. Optical Combiners

The summation in Eq. (1) indicates that the signals received by the individual elements must be combined not only with specific delays, but also with proper amplitude weighting terms in order to form the beam pattern according to the desired array design criteria [44]. This can be achieved by properly tuning the coupling ratio among the signals originating from the individual antenna elements. It is desirable to have a combining unit that can be tunable through a wide range of values (coupling factor ideally ranging from 0 to 1). A possible solution can be implemented in integrated optics by employing the Mach–Zehnder interferometer (MZI) structure, which consists of two cascaded 3 dB couplers connected by two optical waveguide branches, with a tunable optical phase shifter in one arm [14].

D. OBFN Architecture

The individual delay elements and combiners described in Subsections 2.B and 2.C can be properly arranged to create different programmable delay

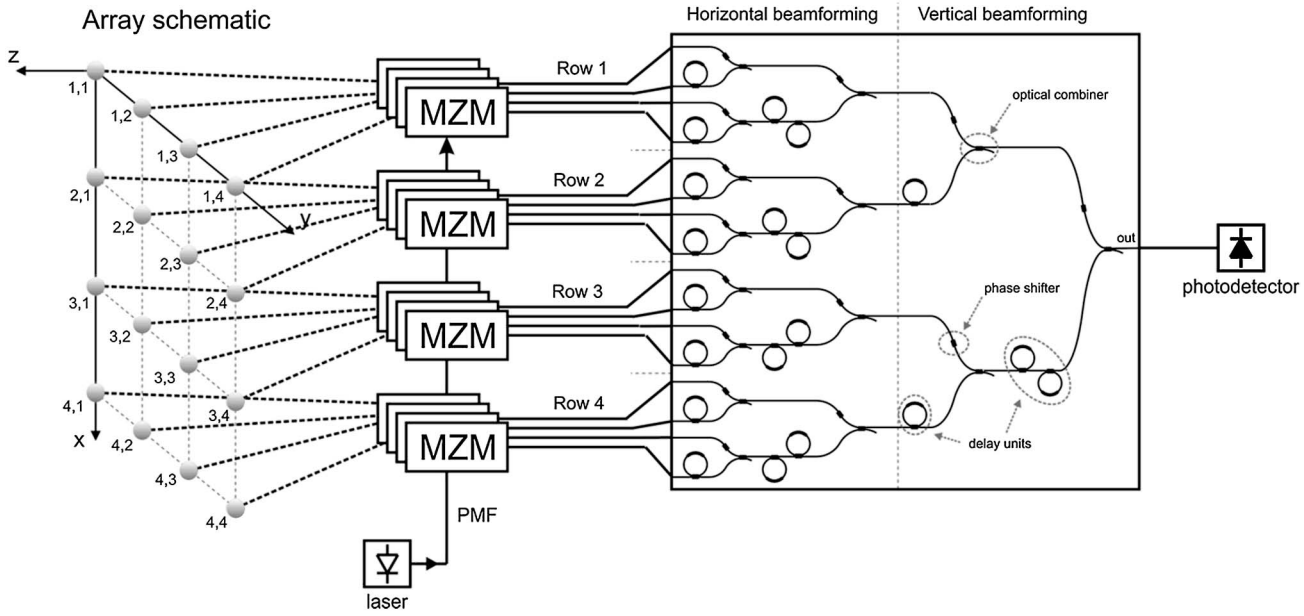

Fig. 2. 16 × 1 OBFN schematic (right), corresponding to a 4 × 4 planar array (left). The position of the ORR delay elements, optical phase shifters, and combiners and their connections are displayed.

paths between each input (corresponding to an individual antenna element) and the output, with tunable amplitude levels. We employ a binary-tree architecture to generate the desired delay and amplitude profile distribution [44], and at the same time to minimize the complexity of the network, as shown in [13,45].

The specific application described in this paper used a 4 × 4 planar array for the complete 400 to 1500 MHz frequency band [36], for which the architecture shown in Fig. 2 has been designed. The total bandwidth (beyond 100%) can now be processed at once by the optical beamformer, while in the full electronic system it had to be divided into 40 MHz-wide instantaneous subbands [35]. Such a large percentage bandwidth is made possible by the properties of ORR-based delay units, as discussed in Section 1. The network (Fig. 2) has 16 optical inputs, corresponding to the individual antenna elements of the 4 × 4 array, and one optical output. The signals received by the individual antenna elements are converted into optical domain by employing an array of 16 Mach–Zehnder electro-optical modulators (MZM). The optical carrier for each modulator is provided by a single laser source via a 1 × 16 optical splitter. The received RF signals, once transferred to the optical domain, are processed and coherently combined by the beamformer chip. The optical combiners described in Subsection 2.C are placed in such a way to form a binary-tree structure, as shown in Fig. 2. The inputs of the horizontal subarrays, or rows (Fig. 2, left side) are combined by the left section (horizontal beamforming). Their outputs are combined by the right section (vertical beamforming). The optical output is then fed to a photodetector to recover the RF signal. The details on the integration of the OBFN in the system setup will be described in Section 3.

E. Optical Technology and Chip Realization

The beamformer chip has been realized by LioniX B.V. on a silicon substrate. The design of the optical waveguides is based on the TriPleX technology, which has been optimized for low loss and minimum chip area occupation, as described in [14,32,46]. In this design, the limiting factor to footprint reduction was the minimum bend radius of 700 μm, needed to ensure negligible bending losses. In present implementations, the minimum bend radius that can be used before bending losses start to be visible has been reduced by almost a factor of 10 [47]. The low propagation losses, which are as low as 0.2 dB/cm for the most recently measured chip [48], assure that the insertion of the beamformer in the receiver has a negligible effect on the system performance. The effects at the system level of the insertion of the described optical beamforming chip in the receiver have been theoretically analyzed in [13] and for a more general case in [49].

The programmability of the delays produced by the ORR units is based on a thermo-optical tuning mechanism [14]. Chromium heaters are placed on specific locations on the top of the chip and connected via gold electrical lines to dedicated contact pads, to which a specific voltage is then applied. The voltage supplied to each heater can be controlled with high accuracy by means of a dedicated, 14 bit digital-to-analog converter and a DC amplifier array. The applied voltage induces a specific current flow in the heater, which will locally heat up the portions of the chip corresponding to specific waveguide sections.

The temperature change will induce a corresponding change in the refractive index of the medium, which, in turn, will translate into a phase change in the light propagating in the waveguide. The chip

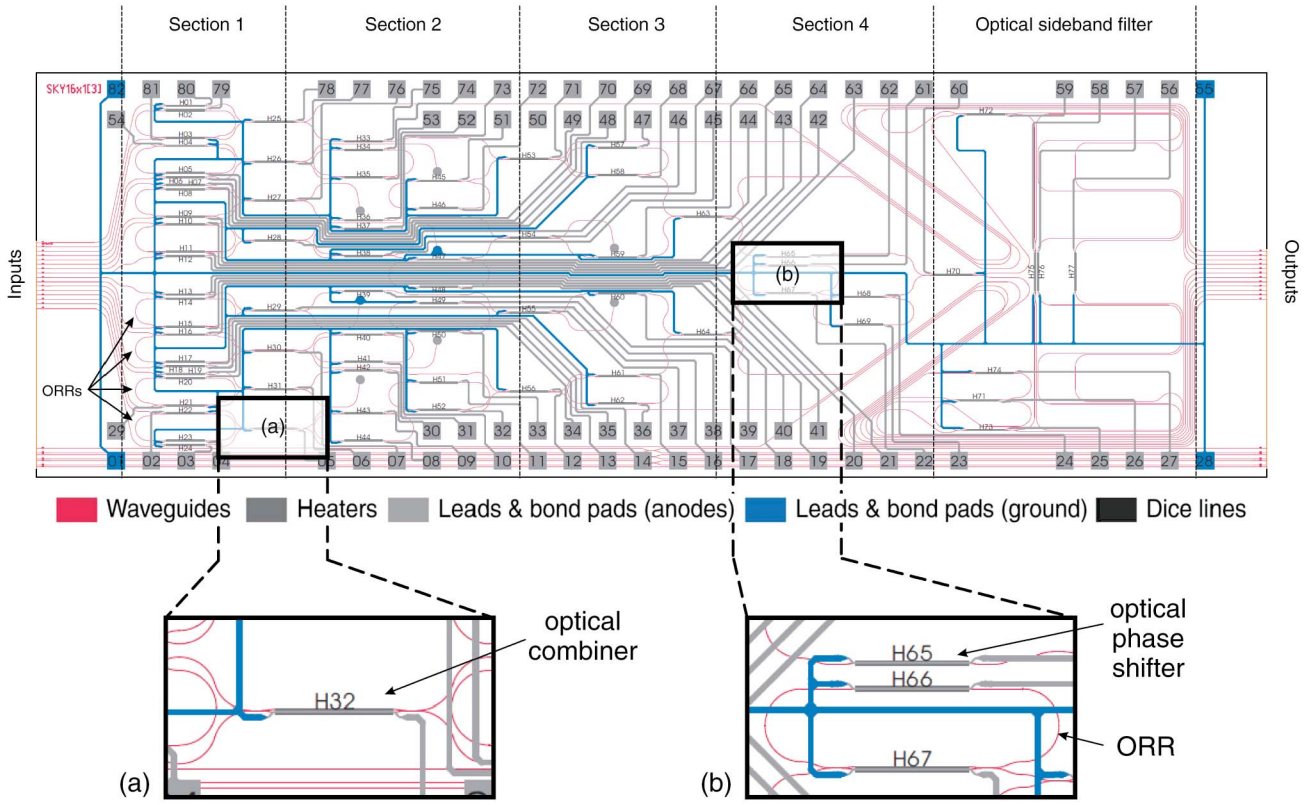

Fig. 3. (Color online) Overview of the 16 × 1 OBFN chip layout (13 × 70 mm). Waveguides, heaters for electro-optical tuning, bond pads, and lines for electrical control are visible. The insets provide a closer view of the tunable combiner (a), of the phase shifter, and of the ORR (b).

temperature is stabilized by a thermal control system.

The layout of the optical beamformer is shown in Fig. 3, where the optical waveguide layout is overlapped with the electrical leads layout. The input waveguides (left) fan out to the inputs of the first beamformer section, where it is possible to recognize the eight ORRs placed on every other input, as shown in the schematic of Fig. 3. The OBFN section 2 contains four pairs of two ORRs each. Sections 3 and 4 contain four rings in total. The optical filter included in the layout is not used in this application and is bypassed during operation. The heater sections used to tune the OBFN are connected to the ground line at one side and to a specific bond pad at the other side, allowing independent control of all the heater elements.

The chip is relatively compact, measuring 13 × 70 mm. It has been pigtailed with two fiber array units (FAU) for ease of testing. The input and the output FAUs contain 16 polarization maintaining single mode fiber pigtails each, which provide an easy access to all the inputs and outputs of the chip. A picture of the packaged chip is shown in Fig. 4, where the input FAU can also be seen.

3. Description of the RF Photonic Integrated System

The wideband, continuous beamsteering capability of the proposed beamformer structure has been demonstrated by a measurement in the near-field antenna test range facility of The Netherlands Institute for Radio Astronomy (ASTRON). The OBFN subsystem has been integrated on the antenna array. The integration and the experimental results are described in the following sections.

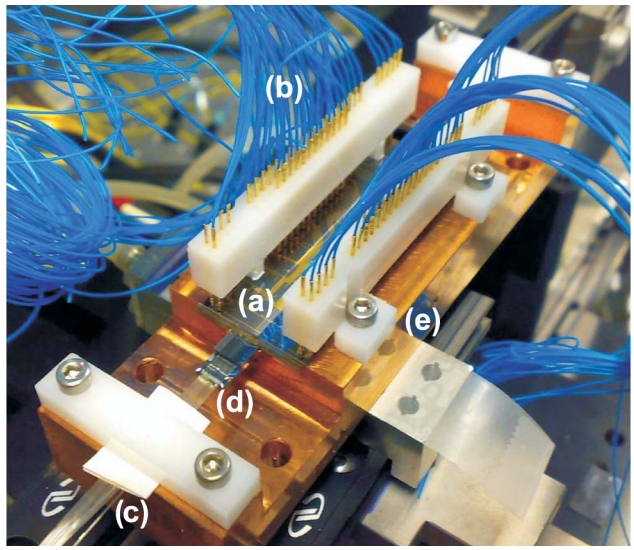

Fig. 4. (Color online) Photograph of the packaged chip (a) with electrical (b) and optical (c) connections. The fiber array unit (d) and the copper block used as support and heat sink (e) are also visible.

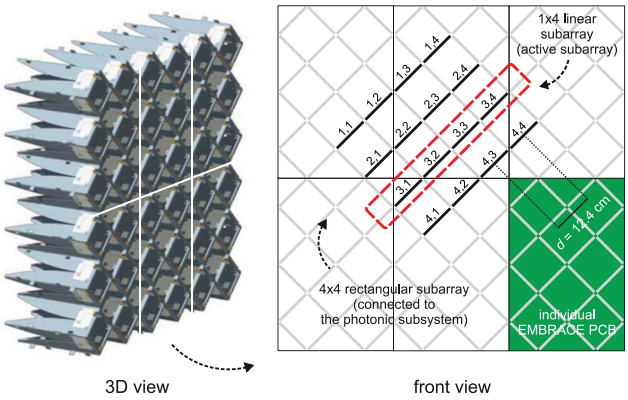

Fig. 5. (Color online) Schematic representation of the antenna tile: 3D view (left), front view (right). The complete tile is built out of six individual printed circuit boards (PCBs). In the front view, each diagonal segment represents one of the Vivaldi antenna elements. The 16 numbered elements are the ones that have been connected to the photonic subsystem (4 × 4 rectangular subarray). The four-element linear subarray used for the demonstration is the one surrounded by the dashed line (1 × 4 linear subarray—active subarray). Its position and orientation with respect to the complete tile are visible here. (3D view: edited from http://www.skads-eu.org).

A. Antenna Array and Front-End

The antenna employed for the demonstration consists of a 4 × 4 elements array of Vivaldi antennas, operating in the 400 to 1500 MHz frequency band [36]. This type of radiating element allows ease of integration and exhibits an active reflection coefficient below −10 dB over the whole frequency band. The 4 × 4 rectangular subarray is a subsection of the EMBRACE tile [35], shown in Fig. 5 (left). Figure 5 (right) indicates the position of the 4 × 4 rectangular subarray with respect to the complete tile.

Each antenna element is connected to a low noise amplifier (LNA), based on a commercially available active device, designed for minimum noise figure and allowing a total system noise temperature well below 100 K [35].

B. Photonic Subsystem

For the demonstration presented here, a 1 × 4 linear subarray of the realized 4 × 4 rectangular subarray has been tested. The direction of the 1 × 4 linear subarray forms an angle of 45 degrees with the sides of the tile, and its position in the complete tile is shown in Fig. 5 (right). The corresponding RF photonic integrated system is schematically represented in Fig. 6 and described below.

The photonic subsystem (Fig. 6) consists of the following main components: laser, erbium-doped fiber amplifier (EDFA), optical splitter array, modulator array, optical beamformer chip, detector, and control and bias electronics.

The RF circuit boards connecting the antenna elements to the active front ends have been modified to allow the integration of the photonic components (Fig. 7). In particular, each of the LNA outputs has been connected to a Mach–Zehnder modulator (Photline MXAN-LN-10), mounted on the same printed circuit board (PCB) as the LNAs, via subminiature A (SMA) connectors. The modulators come in a package with single mode, polarization maintaining (PM) input and output fibers. All the optical components used between the laser and the beamformer employ PM fibers. They have been individually tested and characterized prior to assembling, and their fiber lengths have been equalized by the manufacturer, upon request, for the specific application. This equalization process has been performed in order to match the lengths (thus the delays) among the different channels. The residual unavoidable length differences (in the order of a few centimeters) have been compensated using the programmable delays included in the photonic chip and described in Subsection 2.B. The measured optical insertion loss of each modulator is approximately 4 dB, and the value of half-wave voltage ($V_{\pi,\mathrm{RF}}$) is around 5 V. Slight differences in the optical insertion loss (1 dB maximum) have been observed among the different modulators as well as among the different channels of the 1 × 4 optical splitter array. During assembly, an effort has been made to minimize the imbalances among the different beamformer channels, by careful selection of the MZMs to be connected to the individual outputs of the optical splitter array, thus maximizing the amplitude matching of the beamformer. Any residual amplitude imbalance among the channels was compensated by using the continuously tunable combiners described in Subsection 2.C. After the delay and combining processing in the OBFN, the resulting signal is detected with a photodetector (Agere 2560A, 3 dB bandwidth of 13 GHz and responsivity of 0.8 A/W).

The optical carrier is provided by a high-stability tunable laser (ANDO AQ4321D) set to an optical output power of 4.9 dBm and whose wavelength has been tuned to lie in the center of the optical delay band. The output of the laser is then split into four optical carrier signals by a 1 × 4 optical splitter array (Fig. 6).

The fiber-chip coupling at the input and output of the OBFN introduces a coupling loss of around 6 dB per facet due to the absence of a spot size converter at the fiber-chip interface. An EDFA (gain = 22 dB) is used immediately after the laser to compensate this loss. In future implementations, suitable spot size converters will be introduced to reduce the coupling losses, thus removing the need for optical amplification.

A network analyzer (HP 8753D) is used to measure the RF-to-RF responses (s_{21} parameter) of the individual OBFN paths. Port 1 of the network analyzer is connected to the probe antenna, and the output of the photodetector is connected to port 2 (Fig. 6).

4. Experiment

The optical beamformer can be tuned as desired by using dedicated software. Details on the tuning technique can be found in [14]. The preliminary step for the OBFN tuning consists in setting the desired

bias point for each of the MZM modulators. In this test, a double sideband full carrier (DSB-FC) modulation has been achieved by biasing the modulators at their quadrature point [13]. The required bias voltages have been determined manually for each of the modulators.

A. Delay Settings

Once the bias point has been set for all the modulators, the optical chip can then be tuned to give the proper amplitude and delay settings required to implement the desired beam pattern.

First, a single optical path is isolated by properly tuning the optical combiners to separately set its delay response. A test tone at the frequency of 1000 MHz and power of −30 dBm is generated with the network analyzer and fed into the modulators via the probe antenna. The RF power is set to this value to ensure that the LNAs operate in linear region.

The first step is tuning the delay elements. Given the desired steering angle ϑ for the main lobe, the corresponding required delay difference to be set between adjacent antenna elements is calculated as [44,50]

$$\Delta\tau = \frac{d\,\cos(\vartheta)}{c_0}. \tag{3}$$

d is the interelement distance shown in Fig. 5, and c_0 is the speed of light in vacuum.

The desired delay is then set by employing the ORR-based delay units previously described and visible (with numbering) in Fig. 8. Sweeping the laser wavelength, the resonance frequency of the ORRs can be easily identified and subsequently tuned to match the modulated RF signal band (phase shift method [51,52]).

The desired delay difference $\Delta\tau$ (Eq. (3)) can be obtained by setting the corresponding phase difference at the frequency f of operation, using the relation

$$\Delta\phi_f = \frac{2\pi\Delta\tau}{T} = 2\pi f\Delta\tau. \tag{4}$$

The OBFN paths connected to the subarray in use are the (3,1)–(3,4) as indicated in Fig. 5. First (Fig. 8), the path corresponding to input (3,1) can be isolated by tuning the combiners C5, C11, and C14. The RF phase response of this path is set to 0 degrees and used as a convenient reference for tuning the relative phases of the remaining inputs.

The other paths are then isolated and tuned one at a time. First ring number 5 in the path corresponding to input (3,2) is tuned to give the phase shift $\Delta\phi_{1\ \mathrm{GHz}}$, calculated with Eq. (4), compared to the reference path of input (3,1). Then, with the same procedure, rings 13 and 14 are tuned to set the phase shift to be $2\Delta\phi_{1\ \mathrm{GHz}}$ desired for path (3,3). Similarly, ring 6 is then tuned to add enough delay to achieve in path (3,4) a phase shift of $3\Delta\phi_{1\ \mathrm{GHz}}$.

The method described here allows the beamformer to be programmed to generate a main array beam at an arbitrary pointing angle.

The possibility to achieve good isolation among the different channels is important to guarantee high accuracy for the operation of delay tuning. The RF

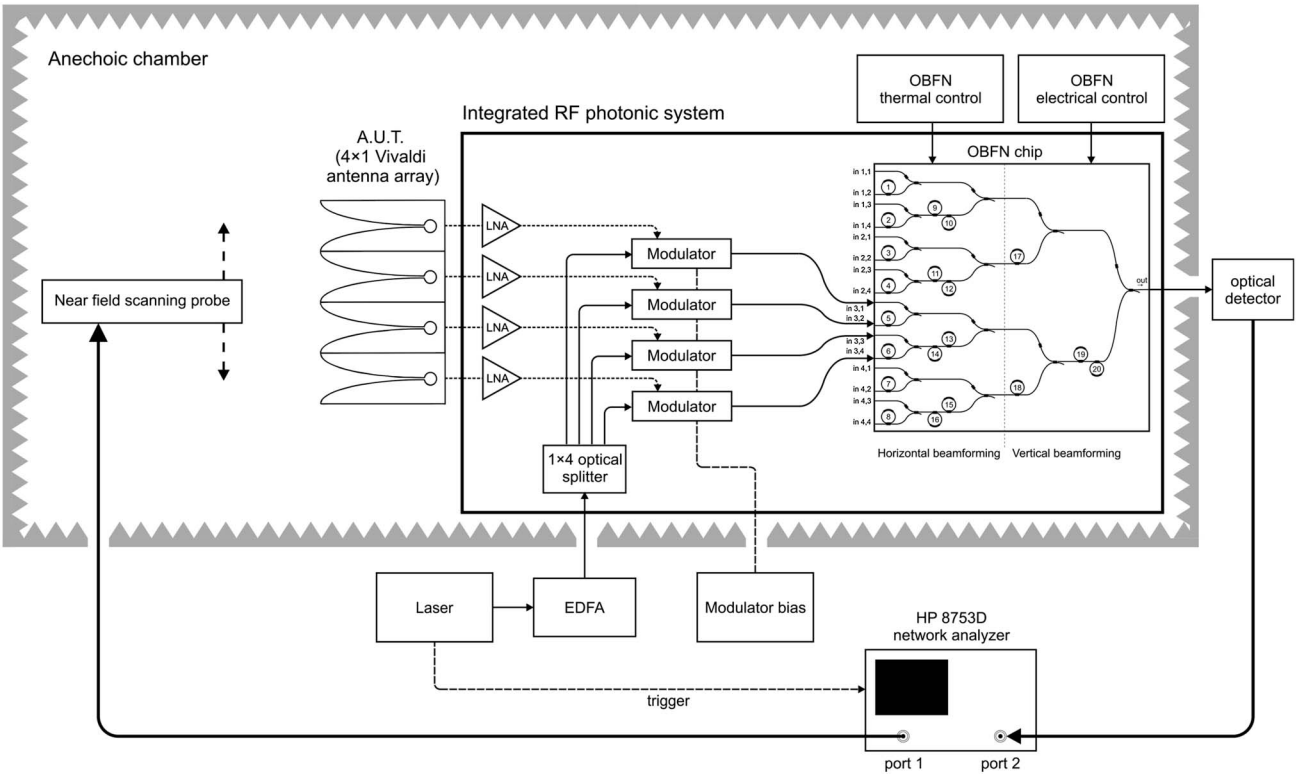

Fig. 6. Setup used in the radiation pattern measurements.

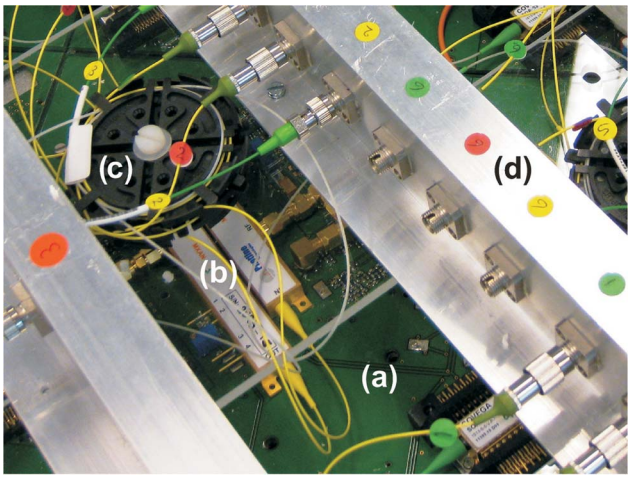

Fig. 7. (Color online) Detail of the back side of the antenna tile. The discrete optical components are mounted on the same PCB as the LNAs (a). Note the modulators (b), the reels (c) for the mechanical support of the fibers, and the panels (d) supporting the optical connectors.

isolation provided with the MZI combiners was tested prior to integration to be in the order of 30 to 40 dB, thus adequate for an accurate calibration of the individual channels. A very high repeatability and stability of the combiner settings was also demonstrated and reported in our previous work [14]. This allowed the combiner settings to be determined prior to integration and then recalled in the calibration phase of the integrated system. Any slight residual deviation from the desired isolation could be compensated for by an additional and highly accurate isolation procedure. This procedure consisted in observing any residual optical interference between the isolated channel and the remaining ones, and in fine-tuning the coupling ratio of the combiners to remove this residual interference, thus providing the best possible isolation among the channels.

B. Amplitude Settings

After the delays have been set as desired with the procedure described above, the second step is the equalization of the amplitude. The individual input–output paths are again isolated, and the magnitude of the s_{21} is compared for the different inputs. Because of the binary-tree architecture of the OBFN, adjacent pairs of channels can be equalized by setting a single combiner. That is, the pairs of inputs (3,1)–(3,2) and (3,3)–(3,4) can be equalized in power by using the couplers C5 and C6 in Fig. 8, respectively. Once those pairs have been individually equalized, the coupler C11 can be used to set the same value for the magnitude of the optical link gain (s_{21}) in the four channels. In this way it is possible to obtain a uniform amplitude excitation.

C. Calibration Accuracy, Stability, and Repeatability

In this demonstration, the beamformer channels have been manually tuned in amplitude and phase for each beam setting. With the described procedure, the amplitude and phase match achieved among the four channels is within 0.5–1 dB in amplitude and below 5 degrees in phase difference (at 1 GHz). For the off-broadside beams, the same high degree of accuracy in the calibration was obtained between the measured and the desired phase differences among the channels, calculated using Eq. (4).

The calibration settings obtained with the described manual tuning approach are stable, and can be saved and recalled at any time. Multiple tests of the same beam setting were repeated at several days of distance from each other and showed very consistent results, giving a further proof of the repeatability of the settings and of the reliability of the thermal stabilization mechanism employed.

D. Optical Phase Synchronization

An aspect that had to be properly considered while performing the measurement was to guarantee the so-called constructive optical interference condition. The presented optical beamformer is a coherent system, meaning that the optical signals have to be combined in phase. Failure to maintain this condition will lead to a loss of the optical signal and, thus, of the RF signal. For this reason, the beamformer includes tunable optical phase shifters before each combining point (see Fig. 8) to adjust the optical phase in each branch in order to achieve constructive interference. Keeping a constructive interference condition at all times can become an issue when using the OBFN in setups where optical fibers are used between the splitting and the combining points, since any mechanical stress and temperature variations on the fibers can create fluctuations of the optical phase, thus an instability problem.

By careful design of the mechanical support and of an enclosure for the fibers, the system is made to work. The following countermeasures have been taken: (1) all the fibers in the setup were fixed using

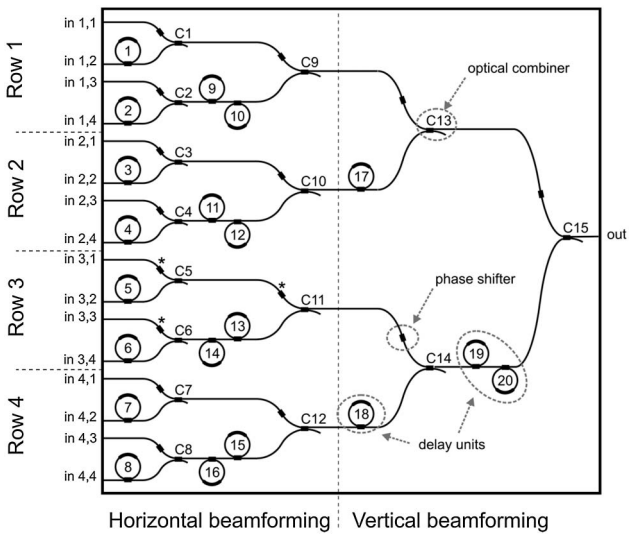

Fig. 8. 16 × 1 OBFN schematic. Numbering of inputs, optical combiners, and ORRs is indicated.

reels and panel mounted connectors with the scope to minimize mechanical vibrations (see Fig. 7); (2) the demonstrator was placed in an air-conditioned anechoic room (Fig. 9) at stable temperature; (3) the whole fiber setup was enclosed in a Plexiglas structure, visible in Fig. 9(b) and (c), which allowed sufficient thermal insulation and avoided fiber vibrations that might have been caused by the airflow present inside the anechoic room due to the air-conditioning system. This solution allowed us to keep the system setup stable for the whole duration of the antenna pattern measurement.

Currently a novel system is being developed, aiming at the integration of the modulators with the OBFN. In this solution, all the signal paths will be integrated on-chip, hence solving the problem of phase instability created by the presence of optical fibers.

5. Antenna Pattern Measurements

Antenna pattern measurements are used to validate the performance of the OBFN. This approach takes into account the setup nonidealities, in contrast to other works that used simulated radiation patterns based on measured scattering parameters [18,22,38]. The latter approach does not take into account several nonidealities, such as the effects of frequency dependence of the beam shape that do not directly depend on the beamformer (e.g., the mutual coupling between the elements, the change in the active reflection coefficient of the antenna with frequency, and the element beamwidth variations), as described in [37, Section 2.1.5].

The integrated array system (OBFN + antenna) was mounted inside the anechoic chamber on a support that could be rotated on the horizontal plane and whose distance from the scanning plane of the near-field probe could be adjusted, in order to measure the radiation patterns (Fig. 9, right). The distance between the probe and the antenna under test has been optimized in order to obtain an accurate measurement of the radiation pattern. The near-field probe is driven by a computer controlled two-axes positioner for automatic near-field scanning (Fig. 9, left). Several test scans have been conducted in order to find the optimal parameters in terms of scanning range and accuracy, i.e., the number of measurement points per scanning direction.

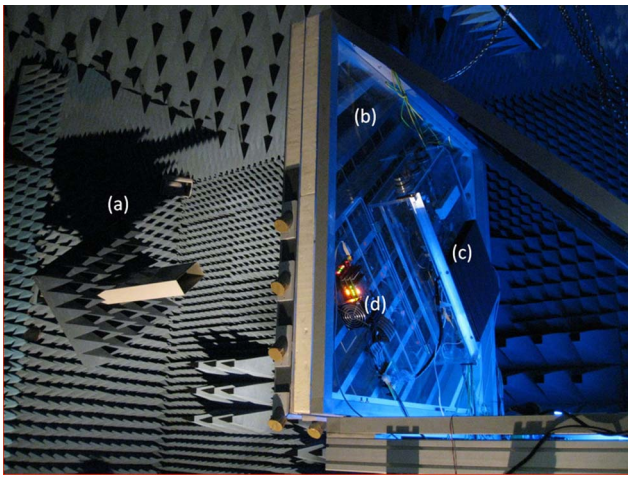

Fig. 9. (Color online) Integrated system mounted in the antenna test range. Left, near-field two-axes scanning probe (a). Right, vertically mounted integrated antenna demonstrator (b, c, d). Different parts of the integrated system are visible. Back side of the antenna tile with integrated RF photonic devices (b). The OBFN chip is inserted in the transparent box visible on the back side of the integrated demonstrator (c). OBFN control electronics (d).

The measurement results are depicted in Fig. 10. Our aim was to test the RF photonic system over the whole band for which it was designed, that is, 400 to 1500 MHz. However, due to limitation in the measurement setup, it was not possible to measure patterns below 1 GHz, which corresponds to the lowest cutoff frequency of the waveguide probes available. For this reason, four frequency points between 1 GHz and 1.5 GHz were measured.

6. Discussion

The measurements have been performed at the frequencies of 1000 MHz, 1150 MHz, 1300 MHz, and 1500 MHz for three different beam pointing directions (0, −11.5, −23.5 degrees) chosen to illustrate the squint-free operation.

The measured radiation patterns are displayed in Fig. 10, normalized to the maximum value. They show a very good agreement with the simulation results (shown by the solid lines) obtained by considering the effect of ideal delays, as in Eqs. (1) and (2). In particular, it is important to note how the position of the main lobe of radiation (indicated by the arrows) does not change across the band for the three different beam pointing directions, thus demonstrating the desired squint-free, or wideband, beamsteering. In the following subsections, a complete analysis of the beam patterns is described, taking also into account the influence of parasitic effects, to demonstrate the squint-free beamsteering.

A. Parasitic Effects in Beam Pattern Measurements

For the broadside beam (0 degrees pointing angle), the sidelobe levels are particularly low, and another interesting phenomenon can be observed. Instead of the expected perfect symmetry around the 0° elevation angle, the sidelobes show lower values for negative pointing angles, when compared to theory, and slightly higher values towards the positive angles, with a corresponding null filling effect that becomes more visible moving toward higher frequencies.

The accuracy of the amplitude and phase matching, resulting from the accurate calibration phase described in Section 4, led us to exclude phase errors as the main cause of the nonideality of the measured radiation patterns. Instead, this asymmetric offset phenomenon is attributed to the parasitic coupling effects, which could not be completely avoided, between the scanning probe and the metal ground plane on which the Vivaldi antenna elements are

mounted for structural reasons. The fact that the 1 × 4 subarray under test is not in the exact center of the metal plane (as visible in Fig. 5) creates the observed asymmetry with respect to the elevation angle. At higher frequencies and steering angles, where the system becomes more sensitive to the described nonidealities and asymmetries of the setup, the parasitic coupling creates higher sidelobe levels and a shift of the leftmost null of radiation, which also affects the shape of the main lobe.

An additional source of pattern degradation is likely to have originated from the mutual coupling between the active array and the unused antenna elements of the tile. The latter were connected to their corresponding LNAs, which were kept biased in the ON state in order to provide the desired terminating impedance to the antenna elements and thus minimize reflections. Nonetheless, not all the antenna elements of the array could be put in place during the measurements. This was due to the structural modifications that had to be performed in order to accommodate the photonic components on the antenna PCBs. The absence of several antenna elements is likely to have had a detrimental effect on the beam pattern and to have been an additional factor to their mentioned asymmetry and null filling effect.

B. Beam Analysis

The discussion described so far clearly shows that the measurements are affected by parasitic phenomena, which could not be removed because they are intrinsic to the measurement setup. The presence of those nonidealities must be carefully considered when analyzing the measured array beam patterns. Given those conditions, to objectively evaluate the performance of the proposed beamformer it is important to isolate as much as possible the effect of those parasitic effects from the analysis of the generated beams. For this scope, we can observe that the nonideal effects on the beam patterns (namely, a shift of the leftmost null of radiation, accompanied by an irregular, asymmetrical shape of the main lobe) are particularly visible for elevation angles around and below −20 degrees, in most of the graphs. This leads us to consider this range as the least reliable to judge the behavior of the array. As a consequence, we need to observe the graphs in the range that shows the patterns being less affected by parasitic effects, thus providing the best possible degree of reliability. For this scope, Fig. 11 shows a magnified view of the nonbroadside beams at −23.5 degrees over the elevation range between −20 and +60 degrees. In this way we can evidence the pattern shape in the elevation

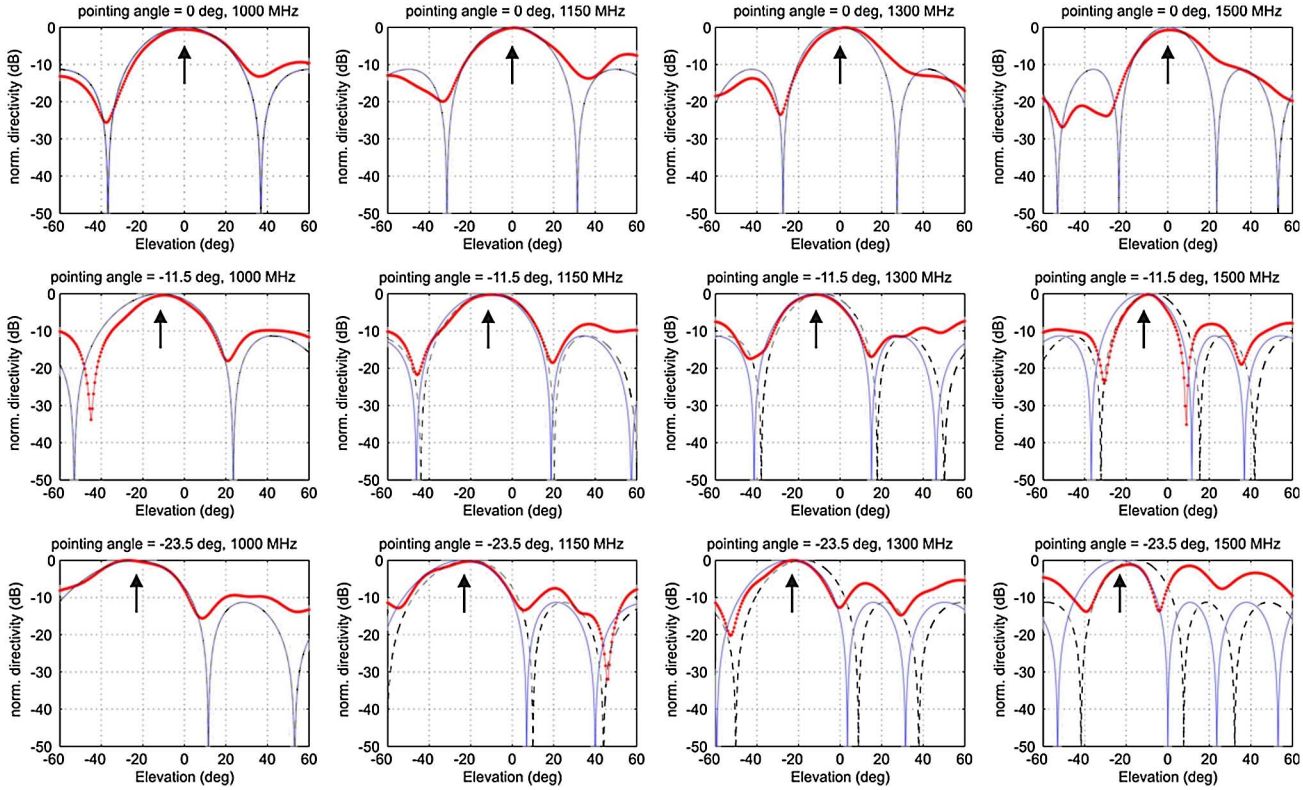

Fig. 10. (Color online) Measured (thick lines) versus simulated (thin solid lines) radiation patterns (E-plane) for three different pointing angles of the main beam: 0 degrees (top), −11.5 degrees (center), and −23.5 degrees (bottom). The measurements are also compared with the patterns that would be obtained in case phase shifters are used (dashed lines). Measurements at four frequencies (left to right: 1000 MHz, 1150 MHz, 1300 MHz, 1500 MHz) show the absence of beam squinting for the main lobe (indicated by the arrows) over the whole frequency range. Note the shift to the right of the leftmost null of radiation and the irregular shape assumed by the main lobe, in several of the measured patterns, as a consequence of parasitic effects in the measurement setup.

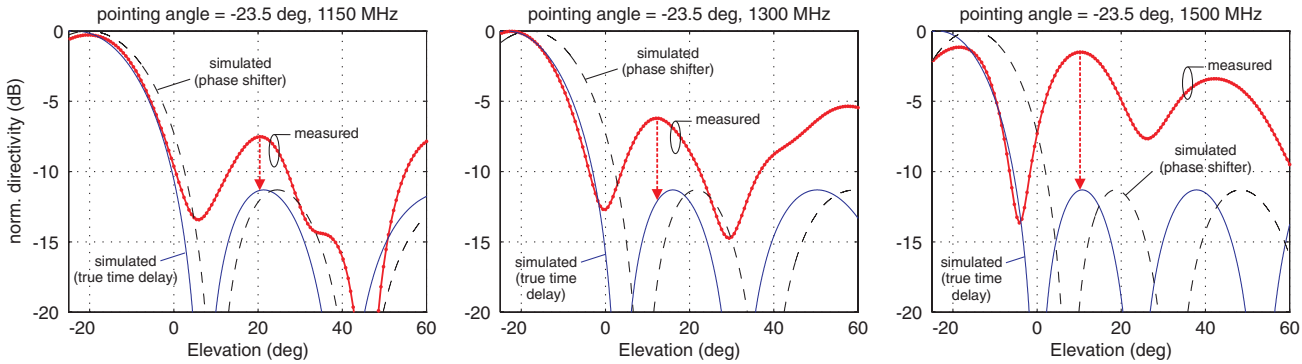

Fig. 11. (Color online) Beam analysis: the measured beam patterns (thick solid lines + dots) are observed and compared with simulations in the elevation range less affected by parasitic effects (−20 to +60 degrees). The comparison shows that the shape of the main lobe and the position of the sidelobes of the measured patterns coincide with the ideal true-time-delay patterns (thin solid lines) and do not show the squint effect suffered by phase shifter based beamforming (dashed lines). This result shows the absence of beam squinting and the utility of true-time-delay beamforming.

range that was less affected by the setup nonidealities, that is, at the right of the main lobe. In this region, the parasitic effects do not disrupt the shape of the main lobe, and the sidelobes are higher but in the expected position. From these plots, it is immediately evident how the measured response

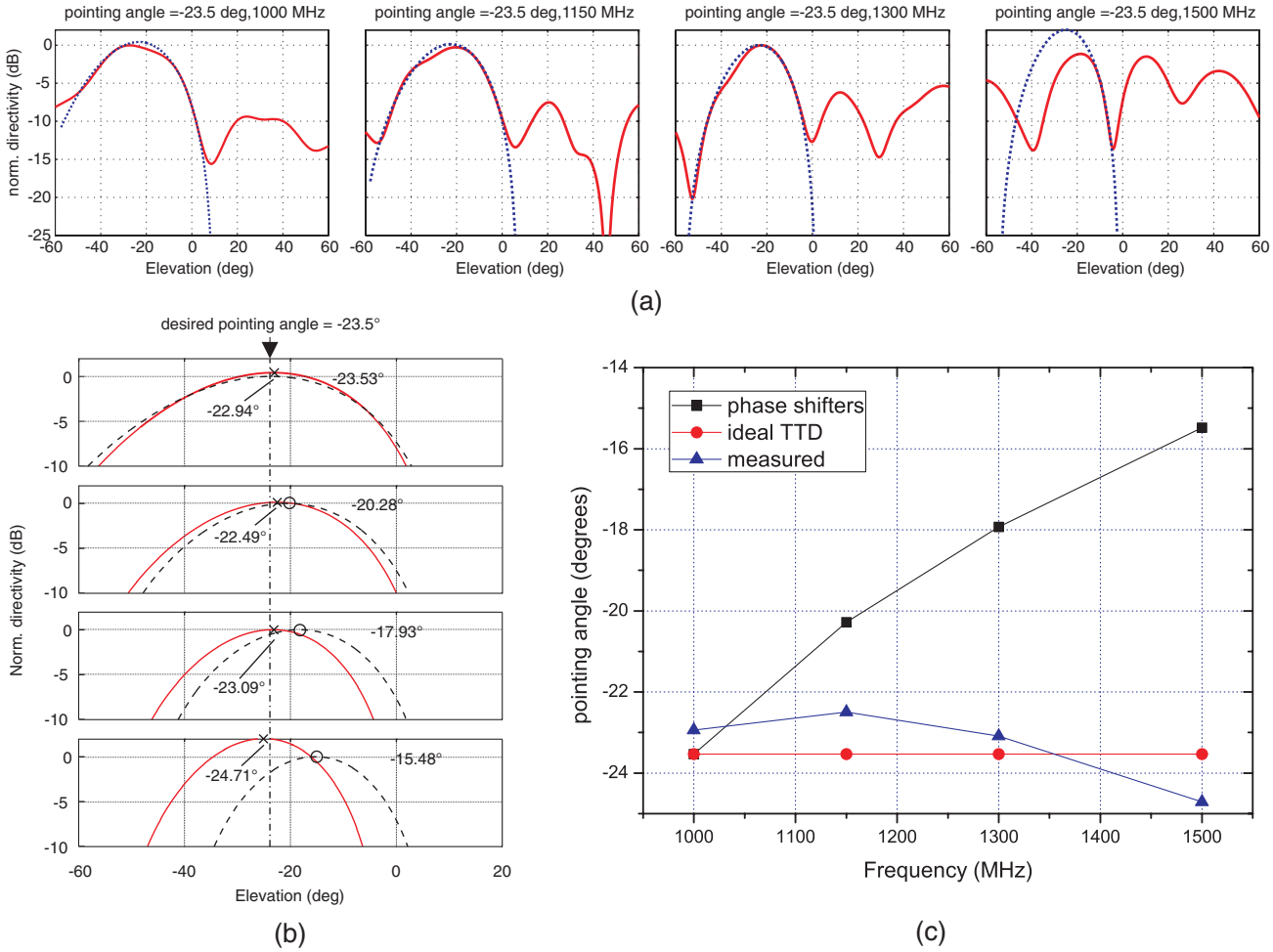

Fig. 12. (Color online) Beam analysis: (a) the asymmetry in the main lobe of radiation caused by parasitic effects (solid line) can be compensated by interpolation (dotted line). (b) The interpolated beams (solid lines) are overlaid on the same angular scale to evaluate the pointing direction at different frequencies, and for comparison with the beams that would be obtained using phase shifters (dashed lines). (c) The pointing direction versus frequency shows a very limited amount of squint when compared to the one that would be obtained using a beamformer based on phase shifters.

(solid thick line + dots) (which at those angles is less influenced by the parasitic effects) shows a good match with the ideal response (solid line), both in terms of position and shape of the main lobe and position of sidelobes and nulls of radiation, and evidences instead a large and clear difference when compared with the squinted response that would be obtained using phase shifters only (dashed line). This gives a proof of the benefit of using time-delay steering even with a steering angle limited to −23.5 degrees from broadside.

In general, a comparison of the pointing direction of the main lobe is the most evident proof of squint-free behavior. Nonetheless, for the same reasons described above, if the parasitic effects are not carefully considered, a misleading result might originate from this analysis. In particular, in Fig. 10 we can observe that the main lobe is affected by asymmetry in shape, showing a clear "bumplike" deviation from its regular quasi-parabolic shape. At −23.5 degrees, this effect moves the maximum to the left (at 1000 MHz) or to the right (at 1150 and 1300 MHz) compared to the position of the maximum that would be expected observing the overall shape of the main lobe. At 1500 MHz the shift of the leftmost null, due to the parasitic effects, completely changes the shape of the lobe. For this reason, the asymmetrical shape of the main lobe would lead to misleading conclusions when the main lobe's maxima would be compared without trying to mitigate the effect of this parasitic effect. The actual pointing direction of the pattern generated by the array can more accurately be estimated by analyzing the overall shape of the lobe, instead of its absolute maximum, which has been shown to be affected by the setup nonidealities (misleadingly moved to the left or to the right). Thus, in Fig. 12(a) we estimate the actual main lobe pointing direction by interpolation of the measured point of the complete main lobe (at 1500 MHz, the interpolation is based on the right part of the main lobe, the left part being strongly affected by the shift of the leftmost null of radiation mentioned before.) At this point, in Fig. 12(b) we can overlay the beams on the same angular scale to evaluate the pointing direction at different frequencies. In Fig. 12(c) the actual pointing directions are compared with the ones that would be generated by using phase shifters, showing the squint reduction and thus the utility of the true-time-delay beamformer. From Fig. 12, it is immediately visible how the percentage variation of the achieved beam pointing direction is much lower than the one for the squinted beams, giving a further proof of the advantage of time-delay beamsteering compared to the use of a phase shifter based beamformer.

These observations demonstrate that the asymmetric behavior is only due to setup nonidealities and that the beamformer is capable of squint-free beamsteering. This is shown over an instantaneous bandwidth of 500 MHz, for a beamsteering of 23.5 degrees, corresponding to an approximately 495 ps delay difference among the opposite elements of the array, or a 14.94 cm distance in air. The bandwidth is only limited by the measurement setup, and is expected to be more than 100% (400–1500 MHz by design) if this limitation were removed.

7. Conclusion

In this work we have reported the system integration and demonstration of a photonically controlled antenna system where the integrated beamformer chip is based on ORR delay units.

The measured radiation patterns show that the beamformer chip is capable of wideband operation. The instantaneous bandwidth is at least 500 MHz and is limited only by the measurement setup.

Future implementations aim to develop a novel fully integrated RF photonic system, eliminating the need for fiber-based components and optical amplification. This will provide prominent benefits in terms of optical phase stability, compactness, and cost.

This work was supported by the Netherlands Ministry of Economic Affairs and the Netherlands Ministry of Education, Culture and Science, within the framework of SmartMix Programme, MEMPHIS Project. M. Burla and K. Dijkstra gratefully acknowledge Michel Arts for the support with the near-field scanning software. Mark Ruiter, Timon Vrijmoeth, Tomas Jansen, Robbin Blokpoel, Jan-Willem van't Klooster, and Jack van Galen are acknowledged for their contributions to the development of the required hardware and software for the chip control system. M. Burla also acknowledges Gennaro Gentile for the fruitful discussion on the measured antenna pattern results.

References

1. M. Tiuri, "Radio astronomy receivers," IEEE Trans. Antennas Propag. **12**, 930–938 (1964).
2. G. Heald, T. Oosterloo, and M. Verheijen, "The science case for APERTIF," presented at the BYU Phased Array Antenna Workshop, Provo, Utah, 3–5 May 2010.
3. D. B. Hayman, T. S. Bird, K. P. Esselle, and P. J. Hall, "Experimental demonstration of focal plane array beamforming in a prototype radiotelescope," IEEE Trans. Antennas Propag. **58**, 1922–1934 (2010).
4. N. A. Riza and J. B. Thompson, *Selected Papers on Photonic Control Systems for Phased Array Antennas* (SPIE Milestone, 1997).
5. A. J. Seeds and K. J. Williams, "Microwave photonics," IEEE J. Lightwave Tech. **24**, 4628–4641 (2006).
6. R. Benjamin and A. J. Seeds, "Optical beam forming techniques for phased array antennas," in *IEEE Proceedings on Microwaves, Antennas and Propagation* (IEEE, 1992), pp. 526–534.
7. D. Dolfi, P. Joffre, J. Antoine, J. P. Huignard, D. Philippet, and P. Granger, "Experimental demonstration of a phased-array antenna optically controlled with phase and time delays," Appl. Opt. **35**, 5293–5300 (1996).
8. A. P. Goutzoulis and J. M. Zomp, "Development and field demonstration of an eight-element receive wavelength-multiplexed true-time-delay steering system," Appl. Opt. **36**, 7315–7326 (1997).
9. R. Palacio, F. Deborgies, and P. Piironen, "Optical distribution of microwave signals for Earth observation satellites," in

Proceedings of IEEE International Topical Meeting on Microwave Photonics (IEEE, 2010), pp. 74–77.
10. D. Yap, O. Efimov, K. Geary, and J. Schaffner, "Compact electro-optic modulator for direct integration into an X-band antenna array front-end," in *Proceedings of IEEE International Topical Meeting on Microwave Photonics* (IEEE, 2010), pp. 35–38.
11. M. Burla, M. R. H. Khan, L. Zhuang, and C. G. H. Roeloffzen, "Multiwavelength optical beam forming network with ring resonator-based binary-tree architecture for broadband phased array antenna systems," in *Proceedings of IEEE/LEOS Benelux Symposium* (IEEE, 2008), pp. 99–102.
12. D. T. K. Tong and M. C. Wu, "Multiwavelength optically controlled phased-array antennas," IEEE Trans. Microwave Theory Tech. **46**, 108–115 (1998).
13. A. Meijerink, C. G. H. Roeloffzen, R. Meijerink, L. Zhuang, D. A. I. Marpaung, M. J. Bentum, M. Burla, J. Verpoorte, P. Jorna, A. Hulzinga, and W. van Etten, "Novel ring resonator-based integrated photonic beamformer for broadband phased array receive antennas—Part I: Design and performance analysis," J. Lightwave Technol. **28**, 3–18 (2010).
14. L. Zhuang, C. G. H. Roeloffzen, A. Meijerink, M. Burla, D. A. I. Marpaung, A. Leinse, M. Hoekman, R. G. Heideman, and W. van Etten, "Novel ring resonator-based integrated photonic beamformer for broadband phased array receive antennas—Part II: Experimental prototype," J. Lightwave Technol. **28**, 19–31 (2010).
15. S. Chin, L. Thevenaz, J. Sancho, S. Sales, J. Campany, P. Berger, J. Bourderionnet, and D. Dolfi, "Broadband true time delay for microwave signal processing, using slow light based on stimulated Brillouin scattering in optical fibers," Opt. Express **18**, 22599–22613 (2010).
16. P. A. Morton and J. B. Khurgin, "Microwave photonic delay line with separate tuning of the optical carrier," IEEE Photon. Technol. Lett. **21**, 1686–1688 (2009).
17. M. Burla, M. R. H. Khan, D. A. I. Marpaung, C. G. H. Roeloffzen, P. Maat, K. Dijkstra, A. Leinse, M. Hoekman, and R. G. Heideman, "Squint-free beamsteering demonstration using a photonic integrated beamformer based on optical ring resonators," in *Proceedings of IEEE International Topical Meeting on Microwave Photonics* (IEEE, 2010), pp. 401–404.
18. T. Mengual, B. Martnez, B. Vidal, and J. Marti, "Wide-band nulling system for antenna array based on a photonic microwave filter and optical delay lines," Opt. Commun. **282**, 3878–3882 (2009).
19. P. J. Matthews, P. Liu, J. B. Medberry, M. Y. Frankel, and R. D. Esman, "Demonstration of a wide-band fiber-optic nulling system for array antennas," IEEE Trans. Microwave Theory Tech. **47**, 1327–1331 (1999).
20. G. Grosskopf, R. Eggemann, H. Ehlers, A. Kortke, B. Kuhlow, G. Przyrembel, D. Rohde, and S. Zinal, "Maximum directivity beam-former at 60 GHz with optical feeder," IEEE Trans. Antennas Propag. **51**, 3040–3046 (2003).
21. R. A. Minasian and K. E. Alameh, "Optical-fiber grating-based beamforming network for microwave phased arrays," IEEE Trans. Microwave Theory Tech. **45**, 1513–1518 (1997).
22. H. Matsuzawa, T. Akiyama, H. Sumiyoshi, T. Iguchi, M. Nagase, Y. Shoji, Y. Fujino, A. Akaishi, and R. Suzuki, "Variable spot scanning antenna using optically controlled beam forming network," in *Proceedings of IEEE International Topical Meeting on Microwave Photonics* (IEEE, 2010), pp. 35–38.
23. S. Blanc, M. Alouini, K. Garenaux, M. Queguiner, and T. Merlet, "Optical multibeamforming network based on WDM and dispersion fiber in receive mode," IEEE Trans. Microwave Theory Tech. **54**, 402–411 (2006).
24. L. Jofre, C. Stoltidou, S. Blanch, T. Mengual, B. Vidal, J. Marti, I. McKenzie, and J. M. del Cura, "Optically beamformed wideband array performance," IEEE Trans. Antennas Propag. **56** , 1594–1604 (2008).
25. A. Molony, L. Zhang, J. A. R. Williams, I. Bennion, C. Edge, and J. Fells, "Fiber Bragg-grating true time-delay systems: discrete-grating array 3-b delay lines and chirped-grating 6-b delay lines," IEEE Trans. Microwave Theory Tech. **45**, 1527–1530 (1997).
26. J. J. Lee, R. Y. Loo, S. Livingston, V. I. Jones, J. B. Lewis, H. W. Yen, G. L. Tangonan, and M. Wechsberg, "Photonic wideband array antennas," IEEE Trans. Antennas Propag. **43**, 966–982 (1995).
27. M. A. Piqueras, G. Grosskopf, B. Vidal, J. Herrera, J. M. Martinez, P. Sanchis, V. Polo, J. L. Corral, A. Marceaux, J. Galiere, J. Lopez, A. Enard, J. L. Valard, O. Parillaud, E. Estebe, N. Vodjdani, M. S. Choi, J. H. van den Besten, F. M. Soares, M. K. Smit, and J. Marti, "Optically beamformed beam-switched adaptive antennas for fixed and mobile broad-band wireless access networks," IEEE Trans. Microwave Theory Tech. **54**, 887–899 (2006).
28. C. Chen, Y. Yi, F. Wang, Y. Yan, X. Sun, and D. Zhang, "Ultralong compact optical polymeric array waveguide true-time-delay line devices," IEEE J. Quantum Electron. **46**, 754–761 (2010).
29. T. Akiyama, K. Inagaki, T. Ohira, and M. Hikita, "Two-dimensional optical signal-processing beamformer using multilayer polymeric optical waveguide arrays," IEEE Trans. Microwave Theory Tech. **49**, 2055–2061 (2001).
30. R. Nagarajan, C. H. Joyner, R. P. Schneider Jr., J. S. Bostak, T. Butrie, A. G. Dentai, V. G. Dominic, P. W. Evans, M. Kato, M. Kauffman, D. J. H. Lambert, S. K. Mathis, A. Mathur, R. H. Miles, M. L. Mitchell, M. J. Missey, S. Murthy, A. C. Nilsson, F. H. Peters, S. C. Pennypacker, J. L. Pleumeekers, R. A. Salvatore, R. K. Schlenker, R. B. Taylor, H. Tsai, M. F. Van Leeuwen, J. Webjorn, M. Ziari, D. Perkins, J. Singh, S. G. Grubb, M. S. Reffle, D. G. Mehuys, F. A. Kish, and D. F. Welch, "Large-scale photonic integrated circuits," IEEE J. Sel. Top. Quantum Electron. **11**, 50–65 (2005).
31. M. K. Smit, Y. S. Oei, F. Karouta, R. Nötzel, J. H. Wolter, E. A. J. M. Bente, X. J. M. Leijtens, van der Tol, M. T. Hill, H. J. S. Dorren, G. D. Khoe, and J. J. M. Binsma, "Photonic integrated circuits: where are the limits?," in *Integrated Photonics Research and Applications Technical Digest* (Optical Society of America, 2005), paper IWB1.
32. L. Zhuang, C. G. H. Roeloffzen, R. G. Heideman, A. Borreman, A. Meijerink, and W. C. van Etten, "Single-chip ring resonator-based 1×8 optical beam forming network in CMOS-compatible waveguide technology," IEEE Photon. Technol. Lett. **19**, 1130–1132 (2007).
33. M. S. Rasras, C. K. Madsen, M. A. Cappuzzo, E. Chen, L. T. Gomez, E. J. Laskowski, A. Griffin, A. Wong-Foy, A. Gasparyan, A. Kasper, J. Le Grange, and S. S. Patel, "Integrated resonance-enhanced variable optical delay lines," IEEE Photon. Technol. Lett. **17**, 834–836 (2005).
34. G. Lenz, B. J. Eggleton, C. K. Madsen, and R. E. Slusher, "Optical delay lines based on optical filters," IEEE J. Quantum Electron. **37**, 525–532 (2001).
35. P. D. Patel, D. W. Kant, E. Wal, and A. van Ardenne, "Phased array antennas demonstrator as a radio telescope—EMBRACE," in *Proceedings of IEEE Antennas and Propagation Society International Symposium 2008* (IEEE, 2008), p. 14.
36. G. W. Kant, P. D. Patel, S. J. Wijnholds, M. Ruiter, and E. van der Wal, "EMBRACE: A multi-beam 20,000-element radio astronomical phased array antenna demonstrator," IEEE Trans. Antennas Propag. **59**, 1990–2003 (2011).
37. R. E. Collins, *Antennas and Radiowave Propagation* (McGraw-Hill, 1986).
38. B. Ortega, J. L. Cruz, J. Capmany, M. V. Andres, and D. Pastor, "Variable delay line for phased-array antenna based on a chirped fiber grating," IEEE Trans. Microwave Theory Tech. **48**, 1352–1360 (2000).
39. J. L. Corral, J. Marti, and J. M. Fuster, "Optical up-conversion on continuously variable true-time-delay lines based on chirped fiber gratings for millimeter-wave optical beamforming networks," IEEE Trans. Microwave Theory Tech. **47**, 1315–1320 (1999).
40. D. B. Hunter, M. E. Parker, and J. L. Dexter, "Demonstration of a continuously variable true-time delay beamformer using a multichannel chirped fiber grating," IEEE Trans. Microwave Theory Tech. **54**, 861–867 (2006).
41. B. Zhou, X. Zheng, X. Yu, H. Zhang, Y. Guo, and B. Zhou, "Impact of group delay ripples of chirped fiber grating on

optical beamforming networks," Opt. Express **16**, 2398–2404 (2008).
42. P. Quang Thai, A. Alphones, and D. R. Lim, "Limitations by group delay ripple on optical beam-forming with chirped fiber grating," J. Lightwave Technol. **27**, 5619–5625 (2009).
43. C. K. Madsen and J. H. Zhao, *Optical Filter Design and Analysis: A Signal Processing Approach* (Wiley, 1999).
44. R. C. Hansen, *Phased Array Antennas* (Wiley, 1998).
45. M. Burla, C. G. H. Roeloffzen, D. A. I. Marpaung, M. R. H. Khan, and W. van Etten, "A novel design procedure for minimum RF phase error in optical ring resonator based integrated optical beamformers for phased array antennas," in *Proceedings of IEEE/LEOS Benelux 2010* (IEEE, 2010), pp. 245–248.
46. R. G. Heideman, D. H. Geuzebroek, A. Leinse, A. Melloni, F. Morichetti, C. G. H. Roeloffzen, A. Meijerink, L. Zhuang, W. van Etten, E. J. Klein, and A. Driessen, "Low loss, high contrast optical waveguides based on CMOS compatible LPCVD processing," in *Proceedings of 13th European Conference on Integrated Optics* (IEEE, 2007).
47. L. Zhuang, D. Marpaung, M. Burla, W. Beeker, A. Leinse, and C. Roeloffzen, "Low-loss, high-index-contrast Si_3N_4/SiO_2 optical waveguides for optical delay lines in microwave photonics signal processing," Opt. Express **19**, 23162–23170 (2011).
48. D. Marpaung, L. Zhuang, M. Burla, C. Roeloffzen, J. Verpoorte, H. Schippers, A. Hulzinga, P. Jorna, W. P. Beeker, A. Leinse, R. Heideman, B. Noharet, Q. Wang, and B. Sanadgol, "Towards a broadband and squint-free Ku band phased array antenna system for airborne satellite communications," in *Proceedings of the Fifth European Conference on Antennas and Propagation* (IEEE, 2011), pp. 2274–2778.
49. N. M. Froberg, E. I. Ackerman, and C. H. Cox, III, "Analysis of signal to noise ratio in photonic beamformers," in *Proceedings of IEEE Aerospace Conference 2006* (IEEE, 2006).
50. H. Subbaraman, M. Y. Chen, and R. T. Chen, "Photonic dual RF beam reception of an X band phased array antenna using a photonic crystal fiber-based true-time-delay beamformer," Appl. Opt. **47**, 6448–6452 (2008).
51. K. Daikoku and A. Sugimura, "Direct measurement of wavelength dispersion in optical fibres-difference method," Electron. Lett. **14**, 149–151 (1978).
52. D. Marcuse, *Principles of Optical Fiber Measurements* (Academic, 1981), pp. 279–281.